

High angular resolution imaging with stellar intensity interferometry using air Cherenkov telescope arrays

Paul D. Nuñez^{1*}, Richard Holmes², David Kieda³, Stephan LeBohec⁴

^{1,3,4}*University of Utah, Dept. of Physics & Astronomy, 115 South 1400 East, Salt Lake City, UT 84112-0830, USA*

²*Nutronics Inc., 3357 Chasen Drive, Cameron Park, CA 95682, USA*

26 July 2021

ABSTRACT

Optical stellar intensity interferometry with air Cherenkov telescope arrays, composed of nearly 100 telescopes, will provide means to measure fundamental stellar parameters and also open the possibility of model-independent imaging. In addition to sensitivity issues, a main limitation of image recovery in intensity interferometry is the loss of phase of the complex degree of coherence during the measurement process. Nevertheless, several model-independent phase reconstruction techniques have been developed. Here we implement a Cauchy-Riemann based algorithm to recover images from simulated data. For bright stars ($m_v \sim 6$) and exposure times of a few hours, we find that scale features such as diameters, oblateness and overall shapes are reconstructed with uncertainties of a few percent. More complex images are also well reconstructed with high degrees of correlation with the pristine image. Results are further improved by using a forward algorithm.

Key words: techniques: high angular resolution - instrumentation: interferometers - stars: imaging - stars: fundamental parameters

1 INTRODUCTION

Even though Stellar Intensity Interferometry (SII) was abandoned in the 1970's, there has been a recent interest in reviving this technique, mainly due to the unprecedented (u, v) plane coverage that future imaging air Cherenkov telescope (IACT) arrays will provide (CTA Consortium 2010; Maier et al. 2009). The possibility of probing stars at the sub-milliarcsecond scale and visible wavelengths has motivated new developments in instrumentation and simulations, the latter being the focus of this paper.

Recent results obtained with amplitude (Michelson) interferometry have started to reveal stars as extended objects (e.g. Baldwin et al. 1996; Monnier et al. 2007), and with non-uniform light intensity distributions in the milliarcsecond scale. Such interesting results can be further investigated with SII taking advantage of the longer (km) baselines and relative ease of observing at shorter (blue) wavelengths. For example, measuring stellar diameters at different wavelengths, will make it possible to further investigate the wavelength dependence of limb darkening, (Mozurkewich 2003) and thus constrain stellar atmosphere models. Radii measurements with uncertainties

of a few percent, along with spectroscopic measurements are necessary to constrain the position of stars in the HR diagram (e.g. Kervella 2008). With the methods described in this paper, we show that diameters can in principle be measured with accuracies better than 1% when using realistic array configurations for future experiments such as CTA (Cherenkov Telescope Array). As another example we can consider fast rotating B stars, which are ideal candidates for imaging oblateness, pole brightening (Monnier et al. 2007; von Zeipel 1924), radiatively driven mass loss (Friend & Abbott 1986), and perhaps even pulsation modes (Saio et al. 2006). The impact of rotation on stellar evolution is non-trivial, and several studies have been made in the subject (e.g. Martin 1996; Maeder 1997). Images of rotating stars have become available in the past few years (e.g. Monnier et al. 2007; Aufdenberg et al. 2006), and measurements of oblateness with accuracies of a few percent have been made. We will show that this is comparable to what can be achieved with SII using large arrays of Cherenkov telescopes. There is also the case of interacting binaries, for which we can measure angular separation, diameters, and relative brightness. It may even be possible to measure mass transfer (Verhoelst, van Aarle, & Acke 2007). Measurements of the angular separation in binaries is crucial for determining the masses of stars. These masses must be found to within $\sim 2\%$ (Andersen 1991) in order

* E-mail: pnunez@physics.utah.edu

to test main sequence models. With the methods described in this paper, we show that angular separations can be found to within a few percent from reconstructed images. A more convenient and accurate analysis (beyond the scope of this paper) does not require imaging, and should yield sub-percent uncertainties, so that testing main sequence models will become possible with SII.

In preparation for a large-scale SII observatory deployment, several laboratory experiments are in progress (LeBohec et al. 2010). Their main goal is to measure light intensity correlation between two receivers. It is also worth mentioning the *Star Base* observatory (located in Grantsville, Utah) which consists of two 3m light receivers separated by 24 m and which will be used to test high time resolution digital correlators, and to measure the second order degree of coherence for a few stars. Various analog and digital correlator technologies (Dravins et al. 1994) are being implemented, and cross correlation of streams of photons with nanosecond-scale resolution has already been achieved.

Intensity interferometry, unlike amplitude interferometry, relies on the correlation between intensity fluctuations averaged over the spectral band at electronic (nanosecond) time resolution. These averaged fluctuations are much slower than the (femtosecond) light wave period. This correlation is directly related to the complex degree of coherence γ_{ij} as (Labeyrie, Lipson & Nisenson 2006)

$$|\gamma_{ij}|^2 = \frac{\langle \Delta I_i \Delta I_j \rangle}{\langle I_i \rangle \langle I_j \rangle}. \quad (1)$$

Here, $\langle I_i \rangle$ is the time average of the intensity received at a particular telescope i , and ΔI_i is the intensity fluctuation. Measuring a second-order effect results in lower signal-to-noise ratio when compared to amplitude interferometry (Holder & LeBohec 2006). This sensitivity issue can be dealt with by using large light collection areas (such as those available with air Cherenkov telescopes), longer exposure times and baseline redundancy. The low frequency fluctuation can be interpreted classically as the beat formed by neighboring Fourier components. Since SII relies on low frequency fluctuations, which are typically several orders of magnitude smaller than the frequency of optical light, it does not rely on the phase difference between light waves, but rather in the difference between the relative phases of the two components at the detectors (Hanbury Brown 1974). The main advantage is the relative insensitivity to atmospheric turbulence and the absence of a requirement for sub-wavelength precision in the optics and delay lines (Hanbury Brown 1974). The complex mutual degree of coherence γ is proportional to the Fourier transform of the radiance distribution of the object in the sky (Van Cittert-Zernike theorem). However, since with SII, the squared-modulus of γ is the measurable quantity, the main disadvantage is that the phase of the Fourier transform is lost in the measurement process. The loss of phase information poses a severe difficulty, and images have in the past been reconstructed from the bispectrum technique, using monolithic apertures (e.g. Lawrence et al. 1990). The imaging limitations can be overcome using a model-independent phase recovery technique. Even though

several phase reconstruction techniques exist (Fienup 1981), we concentrate on a two dimensional version of the one dimensional analysis introduced by Holmes & Belen'kii (2004), which is based on the theory of analytic functions, and in particular the Cauchy-Riemann equations.

Following recent successes in Gamma ray astronomy, a next generation Cherenkov telescope array is in a preparatory stage. This project is currently known as CTA (Cherenkov telescope array) (CTA Consortium 2010), and will contain between 50 and 100 telescopes with apertures ranging between 5 m and 25 m. In this paper we investigate the sensitivity and imaging capabilities of SII implemented on such an atmospheric Cherenkov telescope array. We start with a discussion of sensitivity (section 2), followed by a discussion of simulating noisy data as would be realistically obtained with such an array (section 3). Since data have a finite sampling in the (u, v) plane, we discuss our method of fitting an analytic function to the data in order to estimate derivatives which are needed for phase reconstruction (section 4). We then briefly discuss phase recovery (section 5) and proceed to quantify the reconstruction quality using several criteria. We start with the simple case of uniform disks (section 6.1) and progressively increase the degree of image complexity by including oblateness (section 6.2), binary stars (section 6.3), and obscuring disks and spots (section 6.4).

2 SENSITIVITY

The signal to noise ratio (SNR) for an intensity correlation measurement depends on the degree of correlation γ , the area A of each of the light receivers, the spectral density n (number of photons per unit area per unit time, per frequency), the quantum efficiency α , the electronic bandwidth Δf , and the observation time t . The SNR can be expressed as (Hanbury Brown 1974)

$$SNR = n(\lambda, T, m_v) A \alpha \gamma^2 \sqrt{\Delta f t / 2}. \quad (2)$$

The spectral density n is related to the visual magnitude m_v of the star as well as its temperature T and observing wavelength λ . The spectral density $n(\lambda, T, m_v)$ is the number of black body photons per unit area, per unit frequency and per unit time. The dependence of the visual magnitude m_v is found by recalling that the flux for a 0th magnitude star with a temperature of 9550°K observed at 550 nm is $3.64 \times 10^{-23} \text{ W m}^{-2} \text{ Hz}^{-1}$ (Bessell 1979). This in turn corresponds to a spectral density of $10^{-4} \text{ m}^{-2} \text{ s}^{-1} \text{ Hz}^{-1}$. The spectral density as a function of temperature (for different visual magnitudes and observing wavelengths) is shown in Fig. 1, and we see that at constant visual magnitude and observing wavelength, higher temperatures correspond to higher spectral densities. We find that the increase in temperature $\Delta T(\lambda, T, \Delta m_v)$ is approximately $\frac{\lambda k T^2}{hc} \Delta m_v$ for the range of temperatures and wavelengths considered in Fig. 1. For example, at 400 nm, a decrease of 1 visual magnitude is equivalent to increasing the temperature of the star from 5000 K to 5700 K. For this reason high temperature objects are easier targets for SII.

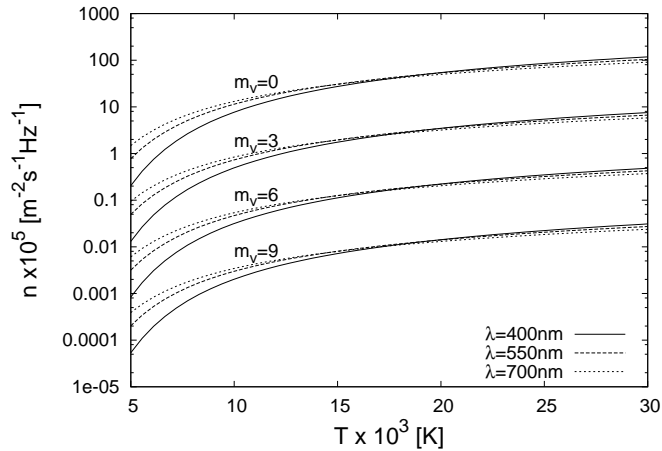


Figure 1. Spectral density as a function of temperature for several different visual magnitudes and observed wavelengths. Atmospheric absorption as a function of the wavelength is not taken into account.

We use a preliminary design of the CTA project as an array configuration (Bernlöhr 2008), which is shown in Fig. 2. This array contains $N = 97$ telescopes and $N(N - 1)/2 = 4646$ baselines (many of which are redundant) which are shown in Fig. 3. Each detector is assumed to have a light collecting area of 100 m^2 and a light detection quantum efficiency of $\alpha = 0.3$. Using a λ/D criterion, we find that the largest baselines of 1.5 km resolve angular scales of $\sim 0.05 \text{ mas}$ at 400 nm . The smallest 48 baselines of 35 m resolve angular scales of $\sim 2 \text{ mas}$. However, we show in section 6.1, that the largest angular scales that can be realistically *imaged* with our analysis, in a model independent way, are more determined by baselines of $\sim 70 \text{ m}$. This is because the estimation of derivatives of the phase (needed for phase recovery) degrades as the number of baselines is reduced. Baselines of 70 m resolve angular scales of $\sim 1.2 \text{ mas}$ at 400 nm .

These order-of-magnitude considerations are taken into account when performing simulations and image reconstructions, i.e. the minimum and maximum size of pristine images that can be reconstructed by data analysis, do not go far beyond these limits. More precise array resolution limits are presented in section 6.1 (diameters ranging between $0.06 \text{ mas} - 1.2 \text{ mas}$). By combining these angular scales with the SNR (eq. 2), we obtain Fig. 4. This figure shows the highest visual magnitude, for which photon correlations (with $|\gamma| = 0.5$) can be detected (5 standard deviations), as a function of the temperature, and for several different exposure times. Also shown in Fig. 4, is the shaded region corresponding to angular diameters between 0.03 mas and 0.6 mas ¹, and observable within 100 hrs. From the Figure

¹ These curves of constant angular size can be found approximately by recalling that the visual magnitude m_v is related to a calibrator star of visual magnitude m_0 by: $(m_v - m_0) = -2.5 \log F/F_0$. Here, F and F_0 refer to the flux in the visual band. To express $m_v - m_0$ as a function of the angular size, note that flux is proportional to $\theta^2 T^4$, where θ is the angular size and T is the temperature of the star.

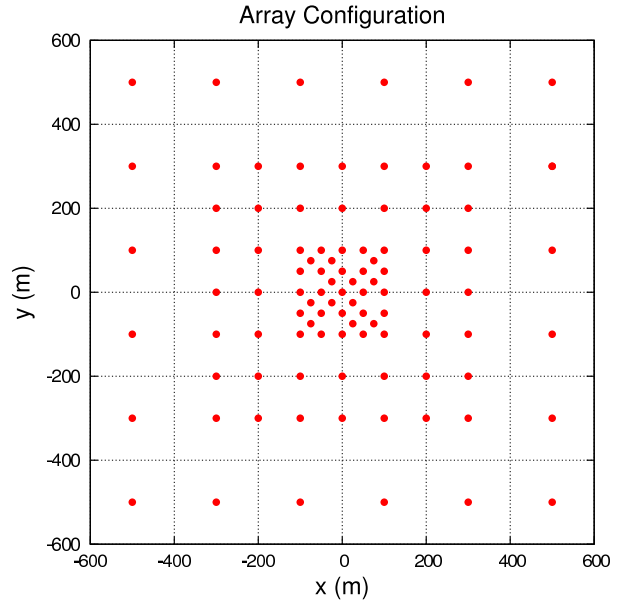


Figure 2. Array configuration used for our analysis.

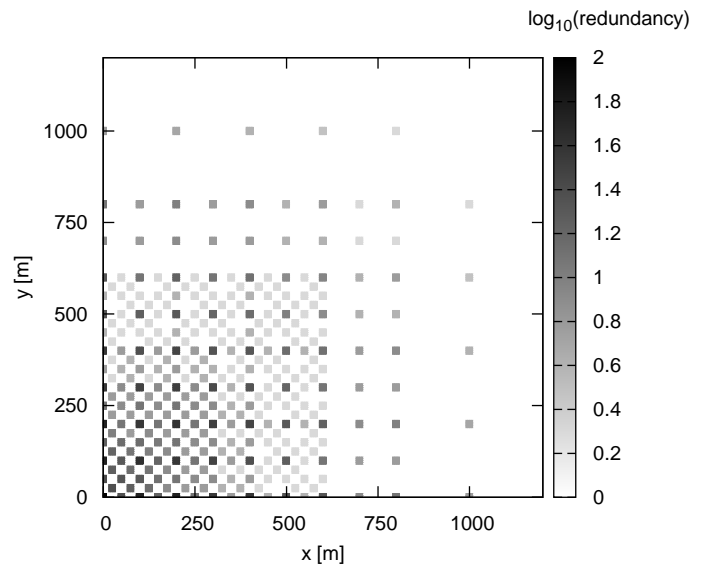


Figure 3. A total of 4656 non-zero baselines are available in the array design used in this study. Gray scale measures the \log of the baseline redundancy. Since the array shown in Fig. 2 is almost symmetric with respect to x and y , only a quadrant of the (u, v) plane is displayed.

we can see how correlations of photons from faint stars can be more easily detected if they are hot. To quantify the number of stars for which photon correlations can be detected with the IACT array, we perform use the JMMC stellar diameters catalog (Lafrasse et al. 2010). We find that ~ 1000 (out of ~ 33000) stars from the JMMC catalog can be detected within 1 hr, correlations from ~ 2500 stars can be detected within 10 hrs, and ~ 4300 can be detected within 50 hrs. In Fig. 2, we show a random sample of 2000 stars (out of ~ 33000) from the JMMC catalog. Interstellar reddening may play a role in reducing the number of measurable targets

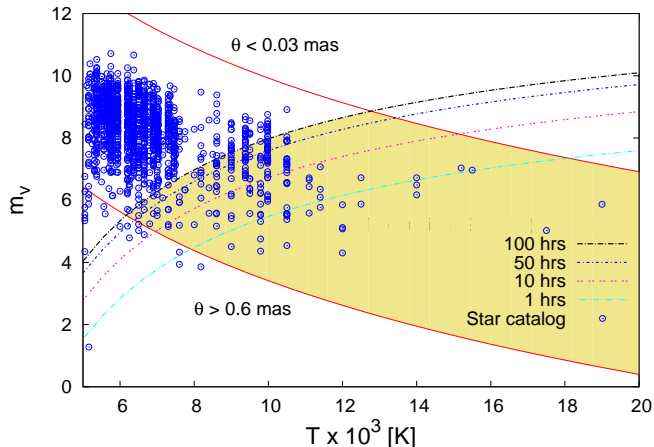


Figure 4. The four parallel curves indicate the maximum detectable visual magnitude as a function of the temperature for several exposure times. Each of these four curves corresponds to 5 standard deviation measurements and $|\gamma| = 0.5$. Also shown is the (shaded) region corresponding to angular radii between 0.03 mas and 0.6 mas, and observable within 100 hrs of observation time. The positions in (T, m_v) space of 2000 stars from the JMMC stellar diameters catalog (Lafrasse et al. 2010) are included.

3 SIMULATION OF REALISTIC DATA

The original “pristine” image consists of 2048×2048 pixels corresponding to $\sim 10 \text{ mas} \times 10 \text{ mas}$ of angular extension and a wavelength of $\lambda = 400 \text{ nm}$. The Fourier transform of the image is then performed via an FFT algorithm and normalized so that its value is one at zero baseline. This results in a Fourier transform sampled every $\sim (8 \text{ m})/\lambda$, i.e. 2×10^7 cycles per radian field-of-view at a wavelength λ of 400 nm. We then find the squared-modulus of the degree of coherence between the members of each pair of telescopes. This is obtained from a linear interpolation of the squared Fourier magnitude in the finely sampled FFT. Diurnal motion is not taken into account in the simulations. Diurnal motion plays a significant role in increasing the (u, v) coverage when exposure times are long. As a consequence there is less (u, v) coverage in the simulations since projected baselines do not drift with time. The smaller (u, v) coverage is however compensated by smaller statistical error in the correlation measurements.

The final step in the simulation phase is the addition of noise to the correlation at each baseline. This noise was found to be Gaussian by performing the time integrated product of two random streams of simulated photons as detected by a pair of photo-multiplier tubes. The standard deviation of the noise added to each pair of telescopes is calculated from eq. 2. In this paper we take the signal bandwidth to be $\Delta f = 200 \text{ MHz}$. An example of simulated data as a function of telescope separation is shown in Fig. 5. This corresponds to a 3^{rd} magnitude uniform disk star ($T = 6000^\circ \text{K}$) of radius 0.1 mas and 10 hrs of observation time. The software used for the simulations, as well as the analysis², was developed in C.

² See sections 4 and 5 for details on the analysis. Some variants of

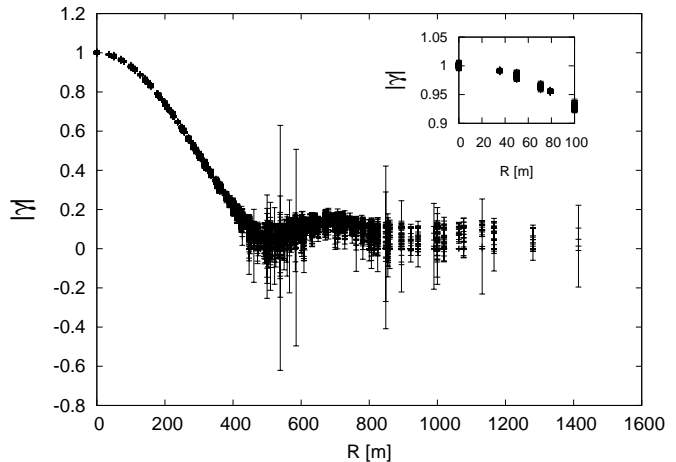


Figure 5. Example of simulated data for a 3^{rd} magnitude uniform disk star ($T = 6000^\circ \text{K}$) of radius 0.1 mas and 10 hrs of observation time. Here we show $|\gamma|$ (instead of the directly measured $|\gamma|^2$) as a function of telescope separation.

4 FITTING AN ANALYTIC FUNCTION TO THE DATA

The estimation of derivatives of the Fourier log-magnitude is at the heart of the Cauchy-Riemann phase recovery algorithm (section 5), and is thus greatly simplified when data is known on a square grid rather than in a ‘randomly’ sampled way as is directly available from observations. Once simulated data are available (or observations in the future), an analytic function is fitted to the data.

An analytic function can be expressed as a linear combination of basis functions. When data $f(x_i) \equiv |\gamma(x_i)|^2$ are available at baselines x_i , with uncertainty $\delta f(x_i)$, the coefficients of the basis functions can be found by minimizing the following χ^2 :

$$\chi^2 = \sum_i \left[\frac{(f(x_i) - \sum_k a_k g_k(\alpha R(x_i)))}{\delta f(x_i)} \right]^2. \quad (3)$$

Each a_k is the coefficient of a basis function g_k . The constant α is a scaling factor, and R is a rotation operator. The scaling factor and rotation angle are found by first performing a two-dimensional Gaussian fit. Finding the appropriate scale and rotation angle has the advantage of reducing the number of basis elements needed to fit the data.

Basis functions which tend to zero at very large baselines, where data are scarce (see Fig. 3), are ideal. For this reason, we use Hermite functions. There are situations where data are more easily fit with a different set of basis functions, e.g. a binary with unresolved members. In such a situation, data do not rapidly tend to zero at large baselines, so the Hermite function fit may contain a large number of elements and result in high frequency noise where

the analysis software were developed in **MATLAB**. All software is available upon request.

data are scarce³. The best choice of basis functions may therefore depend on the structure of the object. However, for consistency, we use the Hermite fit for all the objects that we analyze, and find that it gives reasonably good results.

The χ^2 minimization problem can be turned into a linear system by setting the set of partial derivatives $\frac{\partial \chi^2}{\partial a_k}$ to zero. We typically start with a small number of basis elements, say eight, and only increase the number of basis elements if the optimized reduced χ^2 is greater than some predefined value.

5 CAUCHY-RIEMANN PHASE RECONSTRUCTION

In order to perform a model-independent image reconstruction, the phase of the Fourier transform needs to be recovered from magnitude information only (Labeyrie, Lipson & Nisenson 2006). Since the image is real, the Fourier magnitude is symmetric with respect to the origin in the (u, v) plane. Lack of phase information results in the reconstructed image being arbitrary up to a translation and reflection. We discuss the one-dimensional phase reconstruction prior to developing the two-dimensional analysis. We can start by first approximating the continuous Fourier transform $I(x)$ by a discrete one, i.e. $I(m\Delta x) = \sum_j \mathcal{O}(j\Delta\theta) e^{ijmk_0\Delta x\Delta\theta}$, where $\mathcal{O}(\theta)$ is the image in the sky and k_0 is the usual wave vector. Then it becomes convenient to express the discrete Fourier transform in phasor representation, i.e. $I(z) = R(z)e^{i\Phi(z)}$ where $z \equiv e^{imk_0\Delta x\Delta\theta}$ is complex. Since the discrete Fourier transform is a polynomial in z , the theory of analytic functions can be applied. As a consequence, we obtain the Cauchy-Riemann equations in polar coordinates, which relate the log-magnitude and the phase along the purely real and imaginary axis. If data were available along the purely real or purely imaginary axis, we could directly solve for the phase by integrating along these directions. However, since z , the independent variable of the Fourier transform ($z \equiv e^{imk_0\Delta x\Delta\theta}$), has modulus equal to 1, the phase differences that we seek lie along the unit circle in the complex plane. On the other hand, one can show that by using the Cauchy-Riemann equations, the phase differences along the radial direction in the complex plane⁴ are directly related to the differences in the logarithm of the magnitude which is available from the data (see appendix A for more details).

The procedure to find the phase consists of first assuming a general solution form, then taking differences in the radial direction of the complex z -plane, and finally fitting the data to the radial differences of the assumed solution. A general form of the phase can be postulated by noting that the phase is a solution of the Laplace equation

in the complex plane (applying the Laplacian operator on the phase and using the Cauchy-Riemann equations yields zero). Since the phase differences are known along the radial direction in the complex plane we can take radial differences of the general solution and then fit the log-magnitude differences (available from the data) to the radial differences of the general solution.

We can think of this one-dimensional reconstruction as a phase estimation along a single slice in the Fourier plane. A generalization to two dimensions can be made by doing the same procedure for several slices as described in Fig. 6. In fact, the requirement that a two-dimensional complex function (z_x, z_y) be analytic, is equivalent to satisfying the Cauchy-Riemann equations in both z_x and z_y (Hörmander 1990). The direction of the slices is arbitrary, however for simplicity we reconstruct the phase along an arbitrary set of perpendicular directions in the Fourier plane, and noting that one can relate all slices through a single orthogonal slice, i.e. once the phase at the origin is set to zero, the single orthogonal slice sets the initial values for the rest of the slices.

One can also require that the phase at a particular point in the complex plane be exactly equal when reconstructed along z_x or z_y since each reconstruction is arbitrary up to a constant (piston) and a linear term (tip/tilt). However, imposing this requirement results in a severely over-determined linear system. More precisely, by imposing equality in n^2 points in the complex plane, and having $2n$ slices (each with an unknown constant and linear term), results in a linear system of n^2 equations and $4n$ unknowns. Alternative methods of requiring slice consistency are a possible way of improving phase reconstruction, but are beyond the scope of this paper.

The Cauchy-Riemann approach, with horizontal or vertical slices, and a single orthogonal slice, gives reasonably good results, however, it is not the only possible approach. We have also investigated Gerchberg-Saxton phase retrieval, Generalized Expectation Maximization, and other variants of the Cauchy-Riemann approach. It is premature to conclude which of these approaches is best at this time, given the limited imagery and SNR levels that have been explored. However, the Cauchy-Riemann approach has shown to give better results in a number of cases (Holmes, Nuñez & LeBohec 2010).

6 IMAGING CAPABILITIES

We investigated the imaging capabilities for simple objects⁵, namely uniform disk-like stars, oblate rotating stars, binaries, and more complex images. For most of the objects that we consider, image reconstruction is not necessary, i.e. from the Fourier magnitude alone, one can extract radii, oblateness, relative brightness in binaries, etc. Estimation of these parameters is probably more accurate when extracted directly from Fourier magnitude data only, especially if some

³ A basis set consisting of products of sines and cosines is more suitable in this situation

⁴ If ξ is the real axis and ψ is the imaginary axis, then a difference along the radial direction is $\Delta\xi + i\Delta\psi$ (assuming $\Delta\xi = a\xi$ and $\Delta\psi = a\psi$, where a is a proportionality constant).

⁵ For preliminary study see Nuñez et al. (2010).

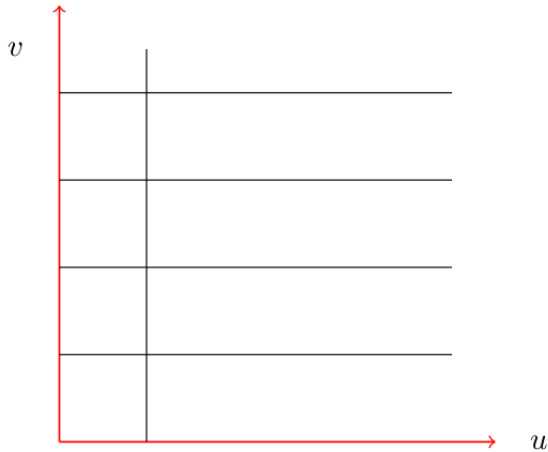


Figure 6. Schematic representation of two-dimensional phase reconstruction approach. Several parallel slices are related to a single orthogonal slice.

a-priori knowledge of the original image is available. However, measuring simple parameters from reconstructed images is the first step in quantifying reconstruction capabilities with IACT arrays. We assume no a-priori knowledge of the images that are being reconstructed, and then do a statistical study of the uncertainties of the reconstructed parameters.

6.1 Uniform disks

In order to quantify the uncertainty in the reconstructed radius, we simulate data corresponding to 6th magnitude stars ($T = 6000^\circ \text{K}$) with disk radii up to 1 mas for 50 hours of exposure time⁶. An example of such a reconstruction is shown in Fig. 7, where the radiance is shown in arbitrary units between 0 and 1. For a uniform disk, the reconstructed phase is null in the first lobe, and we find that the rms deviations from the true phase are approximately 0.19 rad in the null zone. A first look at the reconstruction in Fig. 7 reveals that the edge of the reconstructed disk is not sharp, so a threshold in the radiance was applied for measuring the radius. The radius is measured by counting pixels above a threshold and noting that the area of the disk is proportional to the number of pixels passing the threshold. After experimenting with different radii, we chose the threshold for measuring the radius to be 0.2. We can now compare the simulated and reconstructed radii as is shown in Fig. 8, where each point in the Fig. corresponds to an individual simulation (including noise) and reconstruction. Further optimization in the threshold for measuring the radius should yield a slope even closer to unity in Fig. 8.

Fig. 8 clearly shows that stellar radii ranging from 0.03 mas to 0.6 mas can be measured with uncertainties ranging between sub-percent and a few percent (Figures 9 and 10). It can be seen from Fig. 8, that the uncertainty

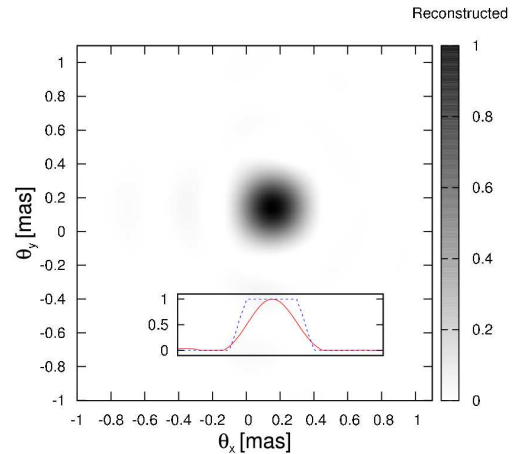


Figure 7. Example of a reconstructed uniform disk of radius 0.1 mas. Also shown is a slice of the reconstructed image (solid line) compared to a slice of the pristine image convolved with the PSF of the array (dashed line).

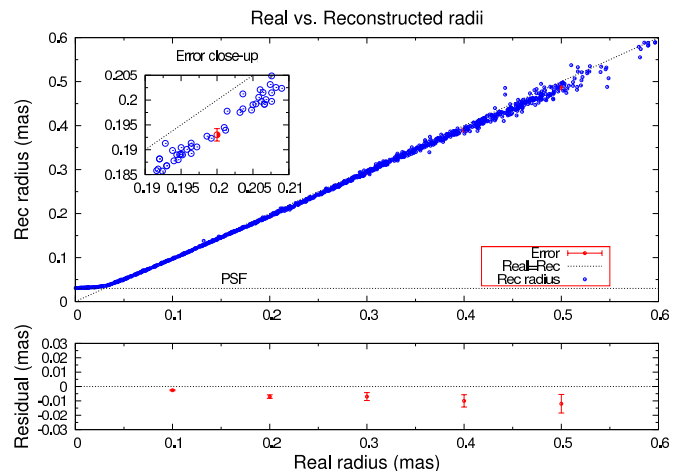


Figure 8. Simulated vs. Reconstructed radii for magnitude 6 stars with 50 hours of observation time (see footnote 6). The top sub-figure shows the uncertainty for a 0.2 mas measurement. The bottom sub-figure shows the residual (Reconstructed-Real) along with the uncertainty in the radius.

increases linearly as a function of the pristine (simulated) radius. This is due to a decrease in the number of baselines that measure a high degree of correlation when the angular diameter increases. As the pristine radius θ decreases, the distance to the first zero in the correlation increases as $\sim \theta^{-1}$, so the number of telescopes contained within the airy disk increases as $\sim \theta^{-2}$. Consequently, decreasing the pristine radius is equivalent to increasing the number of independent measurements by a factor of $\sim \theta^{-2}$. Since the uncertainty decreases as the square root of the number of independent measurements, the error decreases linearly with the radius. For radii above 0.6 mas, there are simply not enough baselines to constrain the Fourier plane information for image reconstruction. For radii greater than 0.6 mas, the distance to the first zero in the degree of correlation is of the order of 100 m, but only baselines at 35 m and 50 m are capable of measuring the Fourier magnitude with more than

⁶ This brightness and exposure time correspond to uncertainties in the simulated data of a few percent. Such long exposure times can be reduced to a few hours as is shown in Fig. 10

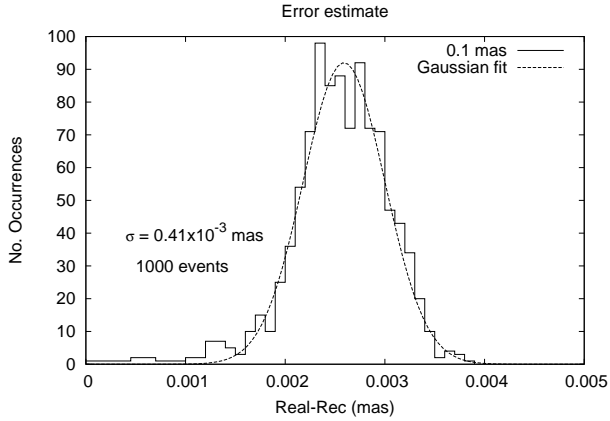


Figure 9. Histogram of real radius minus reconstructed radius for 50 hours of exposure time on a 6th magnitude star ($T = 6000$ K) of 0.1 mas radius.

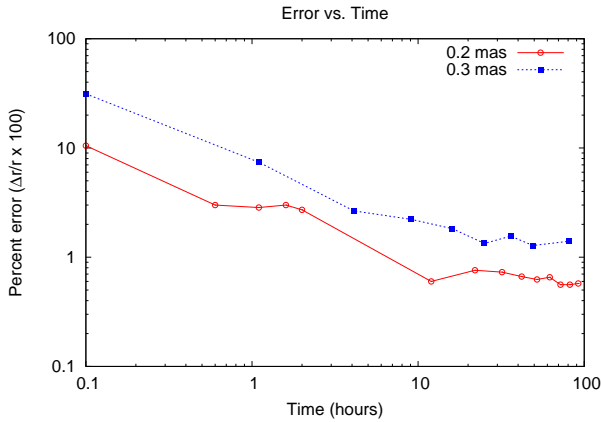


Figure 10. Percent error as a function of time for two reconstructed radii. This error was found by performing several reconstructions for each radius and exposure time, and then taking the standard deviation of the reconstructed radius.

3 standard deviations (see eq. 2). In Fig. 10 we show the relative percent error (RMS of a statistic) as a function of time for two different radii, where it can be seen that a relative error of a few percent is achieved after only a few hours.

6.2 Oblate stars

For oblate stars we use the same magnitude and exposure parameters that are used for disk-like stars. Uniform oblate stars can be described by three parameters: the semi-major axis a , the semi-minor axis b , and the inclination angle θ . Judging from the limitations obtained from reconstructing disks, we produce pristine images whose values for a and b are random numbers less than 1 mas, and choose $1 \leq a/b \leq 2$. The value of the inclination angle θ also varies randomly between 0° and 90° . A typical image reconstruction can be seen in Fig. 11.

After applying a threshold on pixel values as was done for disk shaped stars, the reconstructed parameters are found by calculating the inertia tensor of the reconstructed image. The eigenvalues and eigenvectors of the inertia tensor provide information for the reconstructed values

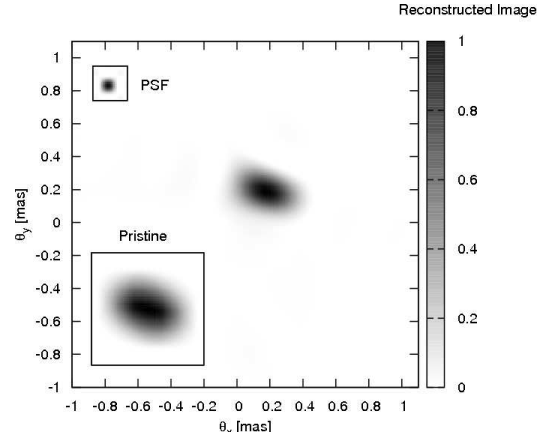


Figure 11. Simulated and reconstructed oblate rotator of magnitude 6 and 50 hours of observation time.

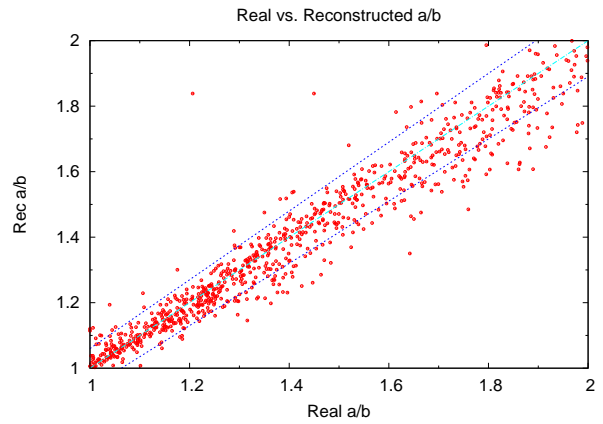


Figure 12. Real vs. reconstructed a/b for oblate stars. The distance between the two linear envelopes is 2 standard deviations. All pristine images that have either $a > 0.5$ mas or $b > 0.4$ mas are not included

of a , b and θ . To do this, we make use of the relation between the matrix eigenvalue and the semi-major/minor axes $I_{xx} = \frac{1}{4}a^2M$, where M is the integrated brightness. A similar relation for I_{yy} holds for the semi-minor axis b .

The resulting reconstructed semi-major/minor axes as a function of their real values have a similar structure as the scatter plot for reconstructed radii shown in Fig. 8, and are well reconstructed up to 0.5 mas within a few percent. In Fig. 12, it can be seen how the uncertainty in the reconstructed oblateness a/b increases with increasing oblateness. As with disk shaped stars (section 6.1), the uncertainty in the reconstructed semi-major/minor axes decreases as the square root of the number of baselines measuring a high degree of correlation. Therefore, the uncertainty in the reconstructed semi-major/minor axes is proportional to $\sim \sqrt{ab}$, and the error in the reconstructed oblateness is proportional to $\sim \sqrt{a/b + a^3/b^3}$.

The reconstructed inclination angle as a function of the pristine angle is shown in Fig. 13, and several factors play a role in the uncertainty of the reconstructed value. For a fixed value of a and b , the orientation of the telescope ar-

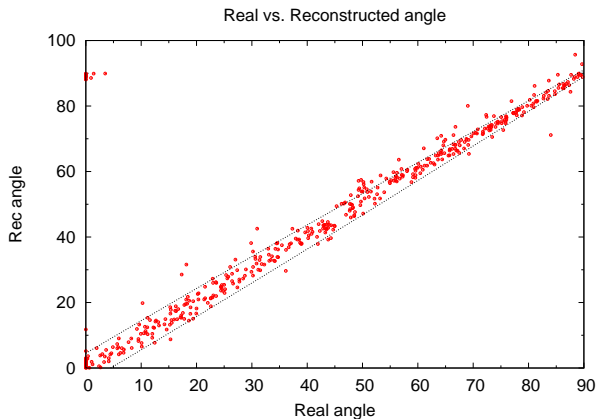


Figure 13. Real vs. reconstructed inclination angle for oblate stars. All pristine images that have either $a > 0.5$ mas, $b > 0.4$ mas or $a/b < 1.1$ are not included. We also note that reconstructed angles are always less than 45° due to the fact that the Fourier magnitude data is the same for pristine images flipped about the x , y or x and y axes. Therefore, for all pristine angles larger than 45° , we replace the reconstructed angle by $\theta'_{rec} = 90^\circ - \theta_{rec}$.

ray with respect to the main lobe of the Fourier magnitude determines the number of baselines that measure a high degree of correlation. The number of baselines that measure a high degree of correlation is greater when the main lobe of the Fourier magnitude is aligned with the x or y direction of the array (see Fig. 2), and is smaller by a factor of $\sim \sqrt{2}$ (assuming a uniform grid of telescopes) when its main axis is at 45° with respect to the array. However, the uncertainty (proportional to spread of points) in Fig. 13 does not appear to be symmetric at 0° and 90° , and is smaller at 90° . This is due to the way the phase is reconstructed, i.e. due to the slicing of the Fourier plane along the u or v directions (see section 5). In the case of Fig. 13, the (u, v) plane is sliced along the u direction, with a single orthogonal reference slice along the v direction. The main lobe of the Fourier magnitude of an oblate star has more slices passing through it when it is elongated along the v direction (corresponding to an inclination angle of 90° in image space), yielding a better reconstruction. This is in contrast to the orthogonal case of 0° , where the main lobe of the Fourier magnitude has a smaller number of slices passing through it.

6.3 Binary stars

Simulated data are generated for 5^{th} magnitude binary stars ($T = 6000^\circ$ K), and an exposure of 50 hours after noting that the uncertainty in the degree of correlation is of the order of a few percent (eq. 2). Binaries stars are parameterized by the radii r_1 and r_2 of each star, their separation d , position angle θ , and relative brightness in arbitrary units between 0 and 1. We generate pristine images with random parameters within the following ranges: radii are less than 0.3 mas, angular separations are less than 1.5 mas, the relative brightness per unit area is less than or equal to 1, and the orientation angle is less than 90° . A typical reconstruction can be seen in Fig. 14.

To measure the reconstructed parameters we identify the two brightest spots whose pixel values exceed a thresh-

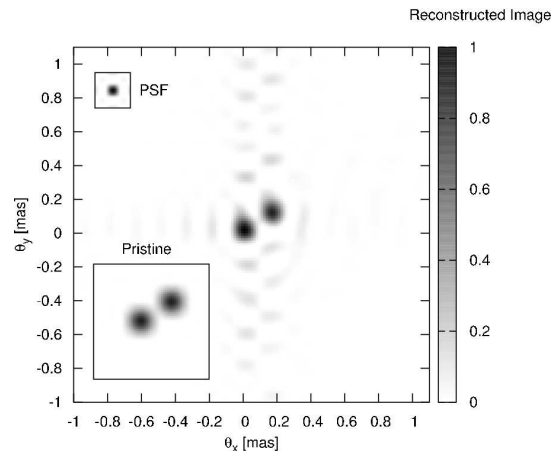


Figure 14. Simulated and reconstructed binary of magnitude 6 and 50 hours of observation time.

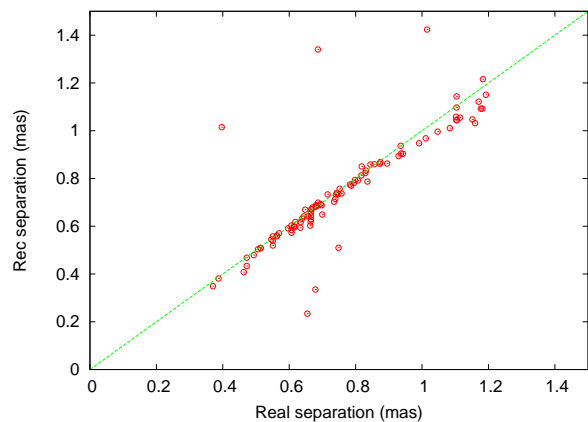


Figure 15. Real vs. reconstructed angular separation in binary stars. Binary stars whose relative brightness is less than 0.3 are not included in this plot.

old of 0.2. We then find the radius for each bright spot and its centroid position. Identifying spots is a non trivial task in noisy reconstructed images and our analysis sometimes fails to identify the “correct” reconstructed spots. For example, a common issue is that close reconstructed spots that are faintly connected by artifacts, are sometimes interpreted as a single spot. It should be again stressed that image reconstruction may not be the best way to measure reconstructed parameters. For example, the data can just as well be fit by the general form of the Fourier magnitude of a resolved binary system (containing only a few parameters).

In Fig. 15, we show reconstructed angular separations as a function of their real values. The reconstructed values of the angular separation are found to within $\sim 5\%$ of their real values and cannot be much larger than what is allowed by the smallest baselines. We find that stars separated by more than $d_{max} \approx 0.75$ mas are not well reconstructed since the variations in the Fourier magnitude start to become comparable to the shortest baseline.

In Fig. 16 we show the reconstructed values of the radii as a function of their pristine values. We find $\sim 10\%$

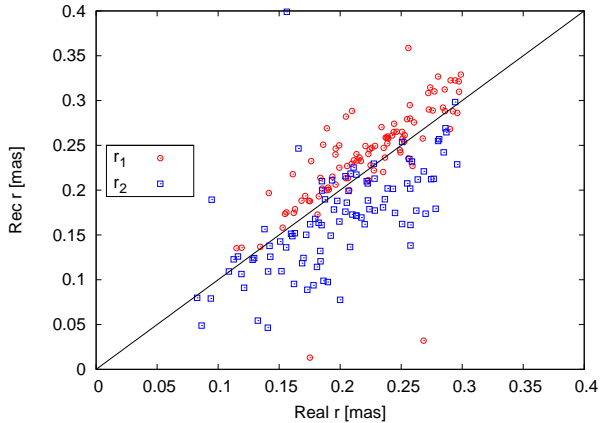


Figure 16. Real versus reconstructed radii for binary stars. We only include cases where one of the members is less than 3 times brighter than the other.

uncertainties in each of the reconstructed radii. Aside from the angular separation, a variable that plays a role in successfully reconstructing pristine radii is the ratio of absolute brightness⁷ of both binary members. When one of the two members is more than ~ 3 times brighter than the other, the fainter star is found to be smaller than its pristine value, and sometimes not found at all when one of the members is more than ~ 10 times brighter than the other. This is in part because the sinusoidal variations in the Fourier magnitude start to become comparable to the uncertainty. For example: a non-resolved binary star with one component 20 times brighter than the other, has relative variations of $\sim 10\%$. With all the redundant baselines, a few percent uncertainty in the measured degree of correlation is sufficient to accurately measure these variations. However, when the binary components are resolved, the relative variations decrease with increasing baseline and baseline redundancy is not sufficient to reduce the uncertainty in the measurement of the Fourier magnitude. This signal to noise issue can of course be improved by increasing exposure time.

There are also issues related to algorithm performance. One such problem has to do with the fit of the data to an analytic function (see section 4). When the scale of the fit (found by an initial Gauss fit) is found to be too small, too many basis elements are used to reconstruct the data, and high frequency artifacts appear in reconstructions. Small initial scales are typically related to the binary separation as opposed to the size of individual components, and it is the latter which correctly sets the scale of the fit. Artifacts may be then mistaken for binary components, and incorrect reconstructed parameters may be found. Results improve significantly when either the correct scale is set or (model-independent) image post-processing is performed (see section 6.5).

⁷ Product of relative brightness per unit area (in arbitrary linear units between 0 and 1) and relative area of both stars

6.4 Featured images

We now present two examples of more complex images, and show that the capabilities can, to a large extent, be understood from results of less complex images, such as uniform disks and binaries. In Fig. 17 we show the reconstruction of a star with a dark band (obscuring disk), corresponding to a 4th magnitude star and 10 hrs of observation time. The metric used to quantify the agreement with the pristine image (bottom left corner of Fig. 17) is a normalized correlation⁸ whose absolute value ranges between 0 (no correlation) and 1 (perfect correlation/anti-correlation). To quantify the uncertainty in the correlation, we perform the noisy simulation and reconstruction several times, and find the standard deviation of the degree of correlation. In the case of Fig. 17, the correlation c is $c = 0.947 \pm 0.001$. Note that the uncertainty in the correlation is apparently small, and the image reconstruction is not perfect, which implies that the reconstruction is not only affected by the SNR level, but also by the reconstruction algorithm performance.

In order to determine the confidence with which we can detect the feature (dark region within the disk), this correlation is compared to the correlation of the reconstruction, and a featureless image, i.e. a uniform disk whose radius matches the radius of the pristine image. This comparison allows us to quantify the confidence with which we actually detect the feature (dark spot). Consequently, the correlation of the reconstructed image with a uniform disk is $c = 0.880 \pm 0.001$, which is lower by 61 standard deviations.

Another example of a complex image reconstruction can be seen in Fig. 18. Here we show the reconstruction of a star with a dark spot, whose correlation with the pristine image is $c = 0.940 \pm 0.001$. We can compare this correlation with the correlation of the reconstructed image and a uniform disk, which is $c = 0.904 \pm 0.001$ (lower by 30 standard deviations).

For both examples, we also calculate the correlation with the pristine image as a function of the angular scale (in mas) of the pristine image. We then find the degree of correlation of each reconstruction and its pristine image, and also the degree of correlation of the reconstruction with a uniform disk. By comparing these two correlation values, we can find the smallest feature that can be reconstructed. Below some point we no longer distinguish between the reconstruction of the featured image and that of a uniform disk. We find that the smallest feature that can be reconstructed is close to 0.05 mas. This can already be seen from the order of magnitude estimate made in section 2 and a comparable value of 0.03 mas is found in section 6.1. When pristine images have angular sizes greater than 0.8 mas, the degree of correlation drops significantly due to lack of short baselines. Note that this value is higher than what is found in section 6.1. This is due to higher signal to noise ratio in

⁸ For two images $A_{i,j}$ and $B_{i,j}$, the normalized correlation $C_{i,j}$ is $C_{i,j} = \text{Max}_{k,l} \left\{ N^{-2} (\sigma_A \sigma_B)^{-1} \sum_{i,j}^{N,N} A_{i,j} B_{i+k,j+l} \right\}$, where σ_A and σ_B are the standard deviations of images A and B .

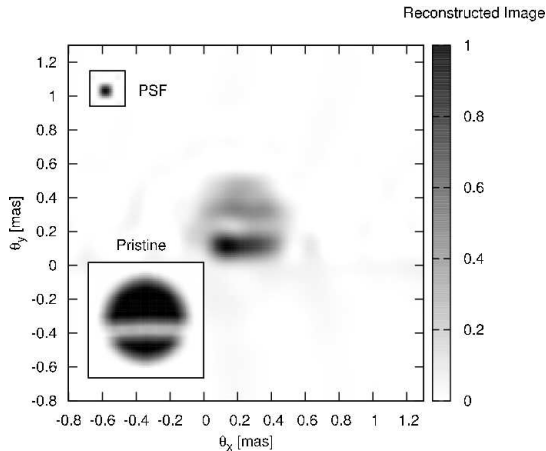


Figure 17. Star with obscuring disk (raw reconstruction). This corresponds to a 4th magnitude and 10 hrs of observation time. The correlation between the real and reconstructed image is $c = 0.947 \pm 0.001$. Note that an inverted gray scale is used.

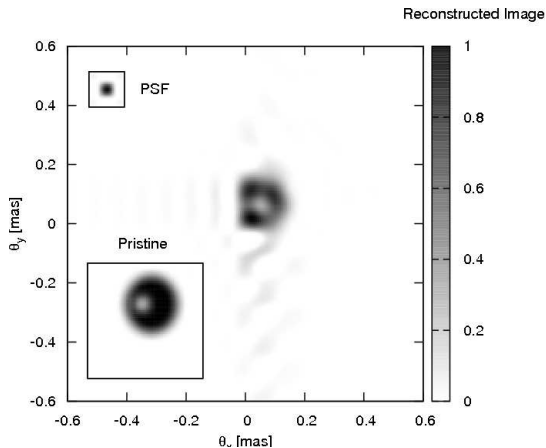


Figure 18. Star with dark spot (raw reconstruction). This corresponds to a 4th magnitude star, 10 hrs of observation time and a degree of correlation of 0.940 ± 0.001 .

the simulated data corresponding to Figures 17 and 18. The resolution limits discussed in turn correspond to $\sim 16 \times 16$ effective resolution elements (pixels).

6.5 Post-processing

Image post-processing is performed in order to improve the raw images presented above. The type of post-processing that is currently being investigated is analogous to the data analysis performed in conventional amplitude interferometry. In this analysis, the image is slightly modified so as to maximize the agreement between the data and the magnitude of the Fourier transform of the reconstructed image. See Thiebaut (2009) for details. Also, one can introduce additional and very general constraints to this maximization procedure, but this is beyond the scope of this paper. Such an analysis depends strongly on the starting image, which can be provided by the analysis presented in this paper. An example of image post-processing performed

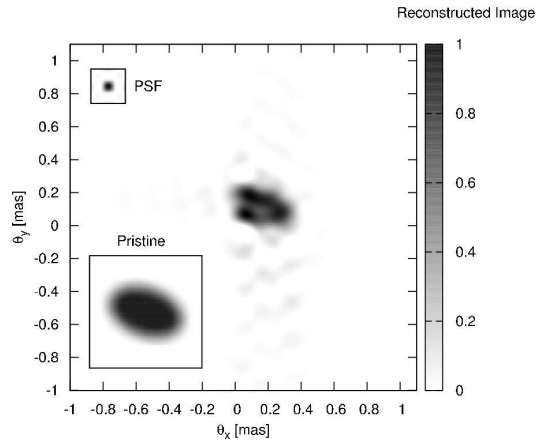


Figure 19. Simulated and (raw) reconstructed oblate rotator of magnitude 3 and 10 hours of observation time. Reconstruction quality is lower when compared to Fig. 11. This is due to high frequency noise in the Hermite fit of the data, and also due to limitations of the phase reconstruction algorithm. Post-processing is applied and Fig. 20 is obtained.

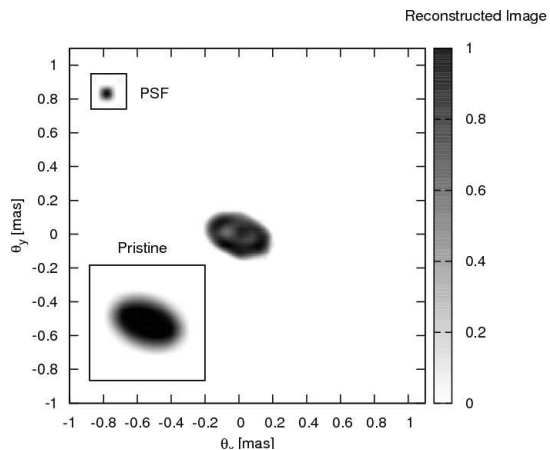


Figure 20. Image post-processing on Fig. 19. The MiRA software was used to optimize on an area $0.3 \text{ mas} \times 0.3 \text{ mas}$.

on the oblate star of Fig. 19 is shown in Fig. 20.

We have performed this type of post-processing on the images in Figures 17 and 18 using the MiRA software (Thiebaut 2009), and we obtain the ones shown in Figures 21 and 22. Aside from optimizing agreement with the data, no additional constraints are imposed. These preliminary results show the overall reduction in noise and improvement in the sharpness of the reconstructed images. A systematic study of the improvements with image post-processing is currently being investigated (Nuñez et al. 2011).

7 CONCLUSIONS

We perform a simulation study of the imaging capabilities at 400 nm of an IACT array consisting of 97 telescopes separated up to a km. This is a preliminary design for the CTA project, expected to be operational in 2018. Our method uses a model-independent algorithm to recover

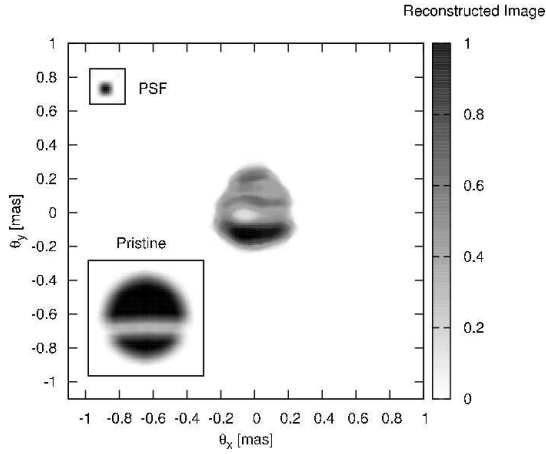


Figure 21. Post processed Fig. 17. The MiRA (Thiebaut 2009) software was used to optimize on an area of $1 \text{ mas} \times 1 \text{ mas}$.

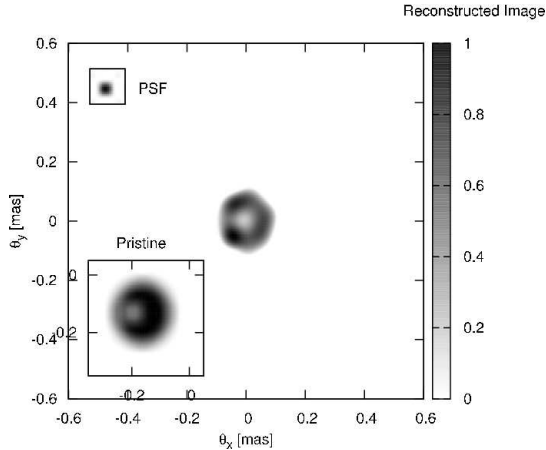


Figure 22. Post processed Fig. 18. The MiRA software was used to optimize on an area $0.3 \text{ mas} \times 0.3 \text{ mas}$.

the phase from intensity interferometric data. We test the method on images of increasing degrees of complexity, parameterizing the pristine image, and comparing the reconstructed parameter with the pristine parameter. We now summarize our results and briefly discuss how fundamental stellar parameters can be constrained with the methods described above.

We first find that for bright disk-like stars ($M_v = 6$), radii are well reconstructed from 0.03 mas to 0.6 mas . Even though using a Cauchy-Riemann based approach to recover images might not be the most efficient way to measure stellar radii, such a study starts to quantify the abilities of measuring other scale parameters in more complicated images (oblateness, distance between binary components, etc.). The range of angular radii that can be measured with a CTA-like array ($0.03 - 0.6 \text{ mas}$) will complement existing measurements ($2 - 50 \text{ mas}$) (Haniff 2001). With the aid of photometry, the effective

temperature⁹ scale of stars within $0.05 - 0.5 \text{ mas}$ can be extended. Multi-wavelength angular diameter measurements will also reveal the wavelength dependence of limb-darkening (Aufdenberg, Ridgway & White 2010), and such measurements can be used to constrain energy transport models as is done in amplitude interferometry (Aufdenberg, Ludwig & Kervella 2005).

For oblate stars, similar results for extracting geometrical parameters are found. Due to the relative ease of SII to observe at short ($\sim 400 \text{ nm}$) wavelengths, measuring fundamental parameters of hot B type stars is possible. B stars are particularly interesting since rapid rotation, oblateness, and mass loss are a common feature. We show that oblateness can be accurately measured, and a next step will be to quantify the capabilities of imaging realistic surface brightness distributions in hot stars. By imaging brightness (temperature) distributions, we will be able to study effects such as limb darkening and mass loss in hot massive stars (Ridgway et al. 2009), as well as gravity darkening (von Zeipel 1924).

Binary stars are well reconstructed when one of the members is not much brighter (three times as bright) than the other, and when they are not too far apart ($\leq 0.75 \text{ mas}$). As with amplitude interferometry, SII, along with spectroscopy, will allow the determination masses and orbital parameters in binary stars. If measured with enough precision ($\leq 2\%$) (Andersen 1991), the determination of the mass can be used to test main sequence stellar models. An advantage of using an array such as the one used in this study, is that individual radii can be resolved. An interesting phenomena to be studied with interacting binary stars is mass transfer (e.g. Zhao et al. 2008), and capabilities for imaging this phenomena can be further investigated.

Two examples of reconstructions of more complex images are presented, and demonstrate the capability to resolve features in the sub-milliarcsecond scale. Results show improvement when post-processing is performed. An optimization procedure improves the image reconstructions found by the methods presented above by maximizing their agreement with the data. A more comprehensive study of reconstructions of complex images is currently being performed.

APPENDIX A. CAUCHY-RIEMANN PHASE RECOVERY

Recall that since SII can only allow to measure $|\gamma|^2$, the phase information is lost, and we would like to recover it for imaging purposes, with only the magnitude information. If we denote $I(z) = R(z)e^{i\Phi(z)}$, where $z \equiv \xi + i\psi$, we obtain the following relations from the Cauchy-Riemann equations¹⁰:

⁹ Defined as $T_{eff} = \left(\frac{L}{4\pi R^2 \sigma}\right)^{1/4}$, where R is the radius, L is the luminosity, and σ is the Stephan-Boltzmann constant.

¹⁰ The C-R equations can be applied because “I” is a polynomial in z .

$$\frac{\partial \Phi}{\partial \psi} = \frac{\partial \ln R}{\partial \xi} \equiv \frac{\partial s}{\partial \xi} \quad (4)$$

$$\frac{\partial \Phi}{\partial \xi} = -\frac{\partial \ln R}{\partial \psi} \equiv -\frac{\partial s}{\partial \psi}, \quad (5)$$

where we have defined s as the log-magnitude. Notice the relation between the magnitude and the phase. By using the Cauchy-Riemann equations we can write the log-magnitude differences along the real and imaginary axes as:

$$\Delta s_\xi = \frac{\partial s}{\partial \xi} \Delta \xi = \frac{\partial \Phi}{\partial \psi} \Delta \xi \quad (6)$$

$$\Delta s_\psi = \frac{\partial s}{\partial \psi} \Delta \psi = -\frac{\partial \Phi}{\partial \xi} \Delta \psi \quad (7)$$

$$(8)$$

If the log-magnitude were available along purely the ξ or the ψ axes, we could solve the previous two equations for the phase.

However, notice that because $|z| = 1$, we can only measure the log-magnitude on the unit circle in the complex space (ξ, ψ) .

In general, we can write the log-magnitude differences along the unit circle as

$$\Delta s_{||} = \frac{\partial s}{\partial \xi} \Delta \xi + \frac{\partial s}{\partial \psi} \Delta \psi \quad (9)$$

$$= \frac{\partial \Phi}{\partial \psi} \Delta \xi - \frac{\partial \Phi}{\partial \xi} \Delta \psi \quad (10)$$

$$= \Delta \Phi_\perp.$$

Here $\Delta \Phi_\perp$ corresponds to phase differences along a direction perpendicular to $\Delta s_{||}$, that is, perpendicular to the unit circle in the $\xi - \psi$ plane. We are however interested in obtaining $\Delta \Phi_{||}$, so that we can integrate along the unit circle.

The general form of Φ can be found by taking second derivatives in eq. (5) and thus noting that Φ is a solution of the Laplace equation in the complex plane.

$$\frac{\partial^2 \Phi}{\partial \xi^2} + \frac{\partial^2 \Phi}{\partial \psi^2} = 0. \quad (11)$$

The general solution of $\Phi(z)$ in polar coordinates (ρ, ϕ) is (Jackson 1998)

$$\Phi(\rho, \phi) = a_0 + b_0 \phi + \sum_j \rho^j (a_j \cos j\phi + b_j \sin j\phi), \quad (12)$$

where terms singular at the origin (ρ^{-j}) have been omitted. These singular terms lead to ambiguous reconstructions including flipped images and have not been found to be essential for most reconstructions.

Now taking the difference of Φ along the radial direction we obtain

$$\Delta \Phi_\perp(\rho, \phi) = \sum_j \rho^j \left(\left(1 + \frac{\Delta \rho}{\rho}\right)^j - 1 \right) (a_j \cos j\phi + b_j \sin j\phi). \quad (13)$$

Note from eq. (10) that the length in the complex plane associated with $\Delta s_{||}$ is $\Delta \phi = |\Delta \xi + i \Delta \psi|$, and that the length associated with $\Delta \Phi_\perp$ is $\Delta \rho = |\Delta \xi + i \Delta \psi|$. Now setting $\rho = 1$, $\Delta \rho = \Delta \phi$, and for simplicity of presentation, expanding for small $\Delta \phi$, we obtain

$$\Delta \Phi_\perp(\phi) = \sum_j j \Delta \phi (a_j \cos j\phi + b_j \sin j\phi). \quad (14)$$

So now the coefficients a_j and b_j can be found using equations (9-10) from the measured $\Delta s_{||}$, and thus Φ can be found in the complex plane, with an uncertainty in a_0 and b_0 . The coefficients a_j and b_j can be calculated by performing the following integrals:

$$a_j = \frac{1}{2\pi j} \int_0^{2\pi} \frac{d\Phi_\perp}{d\phi} \cos j\phi d\phi \quad (15)$$

$$b_j = \frac{1}{2\pi j} \int_0^{2\pi} \frac{d\Phi_\perp}{d\phi} \sin j\phi d\phi \quad (16)$$

Note however that the previous expressions must exist, which is not the general case. More explicitly, if the magnitude is zero, the log-magnitude is singular. When imaging finite objects in image space, there will always be zeros in the magnitude of the Fourier transform. In practice we are always sample limited and nothing prevents us from calculating a_j and b_j approximately.

REFERENCES

- Andersen J., 1991, AAPR, 3, 91
 Aufdenberg J. P., Ludwig H. G., Kervella P., 2005, ApJ, 633, 424
 Aufdenberg J. P. et al., 2006, ApJ, 645, 664
 Aufdenberg J. P., Ridgway S., White R., 2009, astro2010: The Astronomy and Astrophysics Decadal Survey, 2010, 8
 Baldwin J. E. et al., 1996, A&A, 306, L13
 Bernlöhr K., 2008, American Institute of Physics Conference Series, 1085, 874
 Bessell M. S., 1979, PASP, 91, 589
 CTA Consortium, 2010, arXiv:1008.3703
 Dravins D. et al., 1994, Proc. SPIE 2198, 289
 Fienup J. R., 1981, JOSA, 71, 1641
 Friend D. B., Abbott D. C., 1986, ApJ, 311, 701
 Hanbury Brown R., 1974, The Intensity Interferometer, Taylor & Francis, London.
 Haniff C. A., 2001, Galaxies and their Constituents at the Highest Angular Resolutions, 205, 288
 Holder J., LeBohec S., 2006, ApJ 649, 399
 Holmes R. B., Belen'kii M. S., 2004, JOSA 21, 697
 Holmes R. B., Nuñez P. D., LeBohec S., 2010, Proc. SPIE 7818
 Hörmander L., 1990, An introduction to complex analysis in several variables. Elsevier Science
 Jackson J. D., 1998, Classical Electrodynamics, 3rd Edition, by John David Jackson, Wiley-VCH.
 Kervella P., 2008, IAU Symposium, 252, 405
 Labeyrie A., Lipson S. G., Nisenson P., 2006, An Introduction to Optical Stellar Interferometry, by A. Labeyrie, S. G. Lipson and P. Nisenson, Cambridge University Press, Cambridge

- Lafrasse S., Mella G., Bonneau D., Duvert G., Delfosse X.,
Chelli A., 2010, VizieR Online Data Catalog, 2300, 0
- Lawrence T. W., Fitch J. P., Goodman D. M., Massie N. A.,
Sherwood R. J., 1990, Proc. SPIE, 1237, 522
- LeBohec S. et al., 2010, Proc. SPIE, 7734, 7734
- Maeder A., 1997, A&A, 321, 134
- Maier G., preprint(arXiv:0907.5118)
- Martin E. L., Claret A., 1996, A&A, 306, 408
- Monnier J. D., 2007, Bulletin of the American Astronomical Society, 38, 854
- Monnier J. D. et al., 2007, Science, 317, 342
- Mozurkewich D. et al., 2003, ApJ 126, 2502-2520
- Nuñez P. D., Lebohec S., Kieda D., Holmes R., Jensen H.,
Dravins, D., 2010, Proc. SPIE 7734
- Nuñez P. D. et al., 2011, In prep.
- Ridgway S. et al., 2009, astro2010: The Astronomy and
Astrophysics Decadal Survey, 2010, 247
- Saio H. et al., 2006, ApJ, 650, 1111
- Thiebaut E., 2009, New Astron. Rev. 53, 312
- Verhoelst T., van Aarle E., Acke B., 2007, A&A, 470, L21
- von Zeipel H., 1924, MNRAS, 84, 665
- Zhao M. et al., 2008, ApJ, 684, L95